Chapter 3

Chemical turbulence

Traditionally, the term *turbulence* is associated with disordered, highly chaotic fluid flow. However, as the study of turbulent flows is an active field of ongoing research, no generally accepted, rigid definition of hydrodynamic turbulence has been established until today, see *e.g.* Ref. [183]. Over the past decade, it became common to use the word turbulence in a wider sense. In particular, turbulence became a synonym for spatiotemporal chaos, denoting high-dimensional dynamical states with both finite correlation length and time [66].

In the context of reaction-diffusion systems, the term *chemical turbulence* was coined for spatiotemporally chaotic dynamics arising through diffusive coupling in extended systems, where the local dynamics itself is non-chaotic [68]. The crucial role of coupling for these dynamical states is sometimes emphasized by referring to them as *diffusion-induced turbulence*. Prominent examples are phase and amplitude turbulence that are observed, *e.g.*, in a certain parameter range of the complex Ginzburg-Landau equation, see Section 2.4.1.

In this chapter, two cases are reported, where chemical turbulence can be observed in experimental systems. In Section 3.1, results from a quasi-one-dimensional electrochemical system are presented showing transitions from limit cycle oscillations through a phase turbulent regime to space-time defect turbulence. An example of defect-mediated turbulence in a two-dimensional system is introduced in Section 3.2, where observations from the catalytic CO oxidation on Pt(110) are discussed.

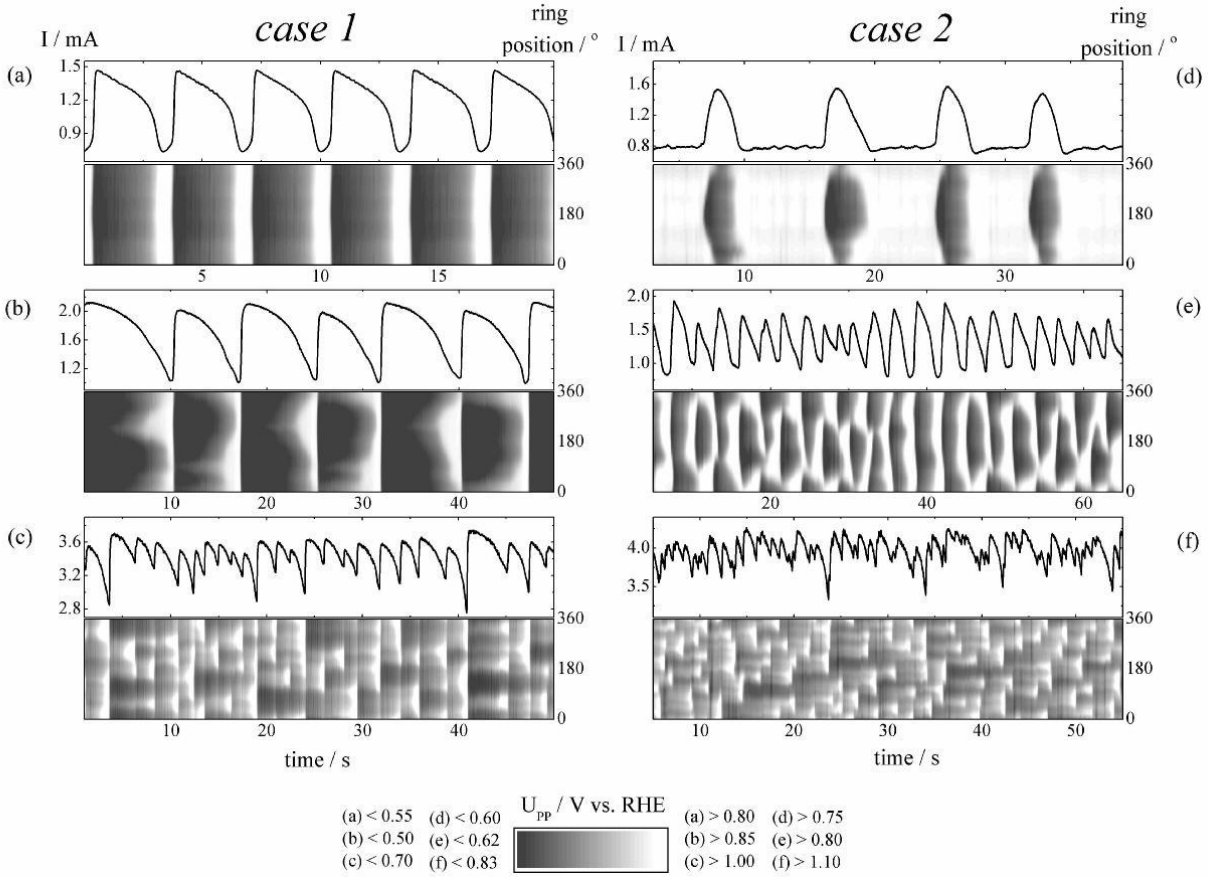

Figure 3.1: Global current time series and corresponding space-time data sets of the interfacial potential ϕ_{DL} at three different voltages for both case 1 (a), (b), (c) and 2 (d), (e), (f). Along the vertical axis of the space-time plots, ϕ_{DL} is displayed in gray scale as a function of angular position on the ring, time runs horizontally. Applied voltages U: (a) 1.06 V, (b) 1.19 V, (c) 2.14 V, (d) 0.82 V, (e) 0.89 V, and (f) 1.54 V. Electrolyte: H_2-saturated, aqueous 0.5 mM H_2SO_4 solution containing 0.1 mM HCl and 0.01 mM $CuSO_4$. A continuous flow of H_2 was maintained throughout the experiments (RHE: reversible hydrogen electrode) [165].

3.1 1D system — Electrochemical oxidation of hydrogen on Pt

In this section, experimental results from oscillatory electrochemical hydrogen oxidation on Pt are analyzed and discussed[1]. The mechanism of the reaction and the experimental setup were introduced in Section 2.3. Here, two series of experiments are presented that were carried out unter identical conditions, differing only in the distance d between

[1] The electrochemical data analyzed in this section was obtained by Hamilton Varela [166].

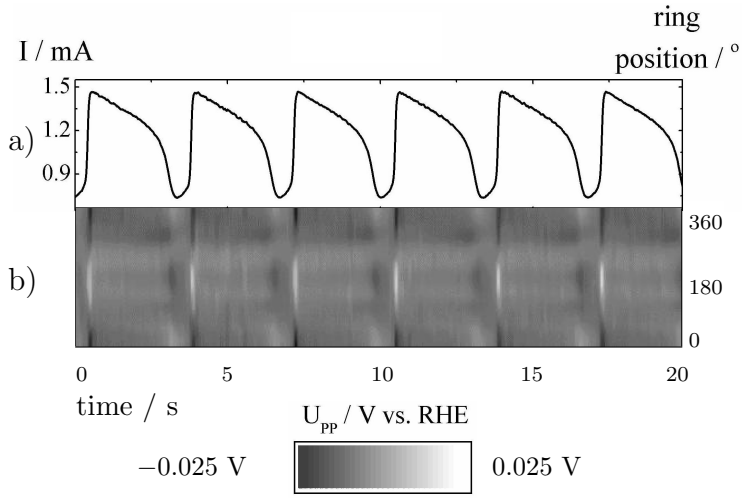

Figure 3.2: (a) Current time series and (b) space-time diagram of the inhomogeneous part of the interfacial potential, $\phi_{\mathrm{DL}} - \langle\phi_{\mathrm{DL}}\rangle_x$, for the data set shown in Fig. 3.1 (a). For parameters see caption of Fig. 3.1. Reproduced from Ref. [166].

working electrode (WE) and counter electrode (CE) in order to impose different ranges of spatial coupling. For the two cases $d = 40$ mm and $d = 5$ mm are chosen, hereafter referred to as case 1 and case 2, respectively. The composition of the electrolyte is given in the caption of Fig. 3.1.

3.1.1 Experimental data

For both large (case 1) and small (case 2) distance between WE and CE the system shows non-stationary states over a broad range of constantly applied voltages U between WE and RE. In both cases, the dynamics was more regular at small values of U, *i.e.* low driving force for the oxidation of hydrogen. With growing U, the spatiotemporal behavior became increasingly complex. Parts of space-time series of the interfacial potential and the corresponding temporal evolutions of the global current are depicted in Fig. 3.1 for three different values of U in each case. In case 1, the current time series exhibits periodic oscillations at low values of U, the interfacial potential being mostly synchronized along the entire electrode (a). Only when subtracting the spatial average at each instant in time, small phase modulations during the fast changes of the current become evident as is shown in Fig. 3.2 (b). With increasing U, the initially small and regular spatial modulations become more pronounced and irregular, see Fig. 3.1 (b), until eventually oscillations break up into domains with decreasing average length scale. A typical state in the strongly irregular regime is depicted in Fig. 3.1 (c).

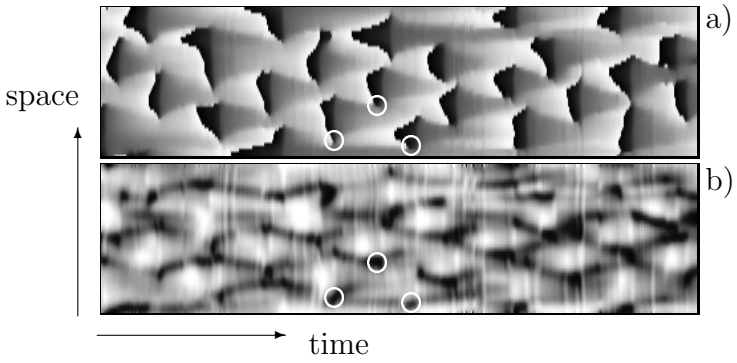

Figure 3.3: (a) Phase and (b) amplitude representations of a spatiotemporal distribution of the interfacial potential $\phi_{\mathrm{DL}}(x,t)$ for case 2 at $U = 1.04$ V. Circles in (a) and (b) exemplify the locations of space-time defects. The displayed time interval is 22.5 s [165].

A similar scenario is observed for a closer distance between the WE and the CE (case 2). Again, the dynamics becomes more irregular with increasing externally applied voltage U. However, in this case, even at the lowest values of U, oscillations are not strictly periodic and show pronounced spatial modulations, Fig. 3.1 (d). With increasing external voltage, the transition to turbulence occurs in a smaller interval of U. Moreover, the length scales of spatial structures in the fully developed irregular regime seem to be smaller than in case 1. Therefore, it can be conjectured that the minimal length scale, below which excitations are damped, is smaller in case 2.

3.1.2 Space-time defects

To characterize the above presented transitions and to analyze the nature of the final spatiotemporally disordered state, the experimental space-time series for the interfacial potential, $\phi_{\mathrm{DL}}(x,t)$, are transformed to a representation in terms of phase and amplitude variables. This description allows comparison of the experimental data with the dynamics of prototypical models for oscillatory systems, in particular, with the CGLE.

In the following, a variant of the analytic signal approach is employed to obtain phase and amplitude of the experimental data sets. The analytic signal is computed by combining the experimental signal and its Hilbert transform. While the phase is directly given as the argument of the analytic signal, the amplitude is additionally normalized by a phase dependent reference amplitude that can be generated by averaging over equidistant phase intervals. Details of this transformation can be found in Appendix A.

An example of phase and amplitude representations is shown in Fig. 3.3 (a) and (b), respectively. They correspond to a strongly irregular data set belonging to case 2. In

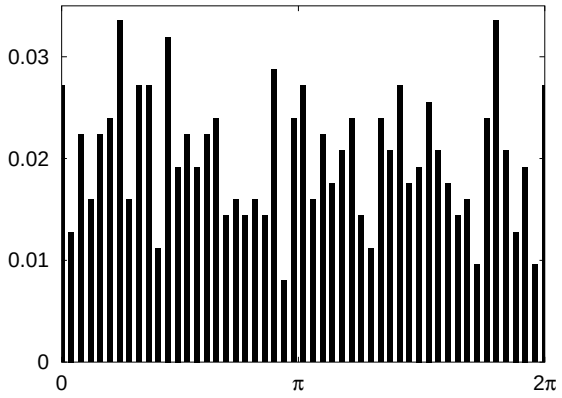

Figure 3.4: Distribution of defect positions along the ring electrode for a strongly turbulent data set belonging to case 2, $U = 1.54$ V. Length of the time series is 314 s.

Fig. 3.3 (a) the phase is shown in a continuous gray scale representation. The discontinuous bright-dark transition lines denote locations where the phase passes from 2π to zero. They are equiphase contours and depend on the definition of the phase, which is fixed except for an arbitrary constant shift. The endpoints of equiphase lines represent space-time defects. Here, abrupt changes in the phase occur. They are associated with a vanishing amplitude as can be confirmed by comparison with Fig. 3.3 (b), see *e.g.* the marked positions. A more precise definition relies on the fact that the integer winding number ν is changed by the presence of a space-time defect, where $\nu = \frac{1}{2\pi}\int_0^L \partial_x \phi(x,t) dx$ with $\phi(x,t)$ denoting the local phase [170]. Thus, in a qualitative respect, the spatiotemporally chaotic dynamics in electrochemical hydrogen oxidation on Pt can be regarded as an experimental analog to turbulence in the one-dimensional CGLE (cf. Section 2.4.1).

For the present analysis, the positions of defects were determined manually by identifying the endpoints of equiphase lines in the phase representations. This was carried out for the different data sets of case 1 and 2. Fig. 3.4 shows the probability distribution of defect positions on the ring accumulated over a time interval of roughly five minutes for a strongly turbulent time series belonging to case 2. Obviously, there are no preferred locations for the emergence of defects on the electrode so that the probability distribution shows random fluctuation around the mean value of 0.02.

The defect densities (averaged number of defects per second) of the different data sets are displayed in Fig. 3.5. Here, the density of defects is plotted versus the applied voltage for case 1 (filled circles) and case 2 (open circles). In both data sets, the defect density increases with increasing voltage starting from zero, indicating that both

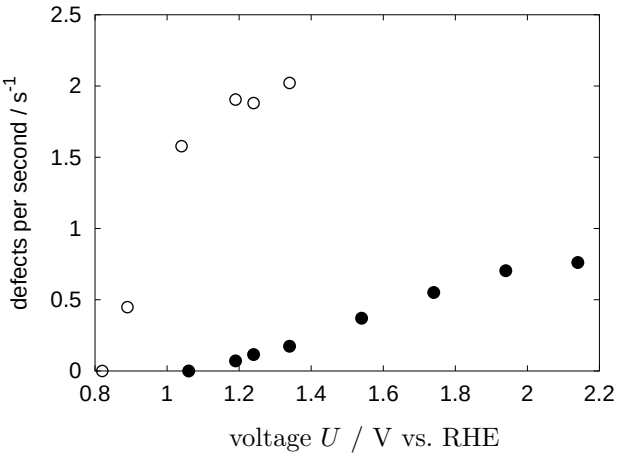

Figure 3.5: Defect density versus externally applied voltage U for case 1 (filled circles) and case 2 (open circles) [165].

series exhibit a transition into a defect turbulent regime. Besides, a second disordered regime dominated by irregular phase modulations in the absence of defects is found for both cases at lower voltages, see Fig. 3.1 (b) and (d). In case 1, moreover, preceding the irregular phase modulated regime, periodic limit cycle oscillations are observed at the lowest value of U as shown in Fig. 3.1 (a). Hence, the two series are indeed experimental manifestations of a transition from phase to defect turbulence. In case 1, even a transition from a periodic limit cycle to defect turbulence via a phase turbulent regime is captured.

From the results displayed in Fig. 3.5, also the differences between the two cases become obvious. Not only does the defect density increase much faster in case 2 than in case 1, but series 2 also reaches a final defect density that is about two and a half times larger than the maximal defect density in case 1. Note that both series were recorded up to values of U at which the Pt surface started to oxidize which determines the upper meaningful limit of the voltage. (The absolute value at which oxidation starts differs in the two cases because of the difference in ohmic cell resistance for the two arrangements of WE and CE). Thus, in case 2, the system shows a higher degree of turbulence than in case 1.

3.1.3 Correlation

A measure of the degree of spatial correlation in the data can be obtained from temporally averaged Fourier spectra of spatial profiles of the interfacial potential. Fig. 3.6

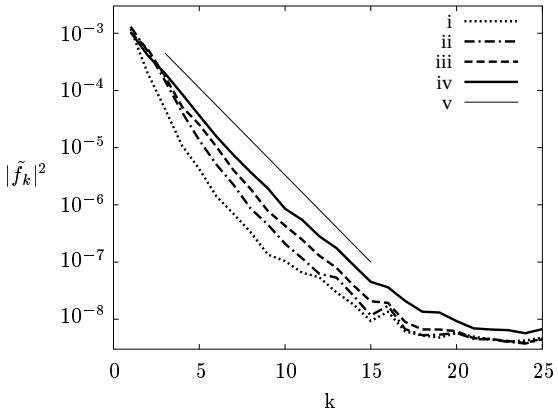

Figure 3.6: Time averaged spatial power spectra of the interfacial potential for different data sets belonging to case 1. The external voltages are 1.19 V (i), 1.54 V (ii), 1.74 V (iii), and 2.14 V (iv). Exponential fit (v) for comparison.

displays a series of such power spectra in a log-lin diagram for different data sets belonging to case 1. With growing external voltage, an increase in the power spectral density is observed for larger wave numbers. This reflects the decreasing characteristic length scales in the spatial distribution of the interfacial potential as the dynamics becomes more turbulent. Besides, the shape of the spectral density approaches an exponential characteristic in the limit of developed defect turbulence. This corresponds to a Lorentzian autocorrelation function, which is the Fourier transform of the power spectrum.

In Fig. 3.7, a comparison of power spectra computed from the most turbulent data series of case 1 (dashed line) and case 2 (solid line) is shown. Both curves decay exponentially within a large range of k. The slopes of the exponential fits (dotted lines) are proportional to the half width at half maximum of the Lorentzian autocorrelation function and, therefore, can be regarded as a measure of the degree of spatial correla-

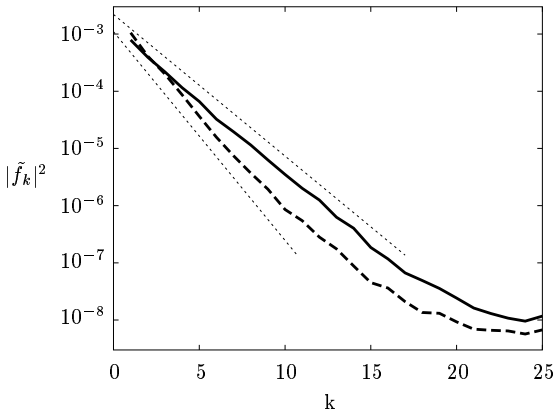

Figure 3.7: Time averaged spatial power spectra in the fully developed defect turbulent regime for both a data set belonging to case 1 (dashed line) and case 2 (solid line), with exponential fits (dotted lines) for comparison. The external voltages are 1.34 V (solid line) and 2.14 V (dashed line) [165].

tion in the data. Thus, the steeper slope in case 1 indicates a larger degree of spatial coherence, supporting the above observation that the length scale of dissipation or damping is larger in case 1. Since the dominant mechanism for damping is provided by the synchronizing effect of spatial coupling, it can be deduced that the coupling range is larger in case 1 than in case 2. This matches the theoretical predictions for coupling in electrochemical systems: According to Eq. (2.18) the range of spatial coupling depends on the distance between WE and CE. For a large distance between the two electrodes a nonlocal coupling is expected that becomes more localized with decreasing distance. The results presented here are the first experimental support of this theoretically predicted peculiarity of spatial coupling in electrochemical systems.

3.2 2D system — Catalytic CO oxidation on Pt(110)

Catalytic CO oxidation on Pt(110) is known to exhibit spatiotemporally disordered, irregular patterns in a wide range of parameters. In general, these dynamical states are loosely referred to as *chemical turbulence*. Although they were already reported together with the first spatially resolved real time observations of concentration patterns on the catalyst surface [46], the precise nature of their dynamics has never been analyzed in detail. This is due to the fact that slow drifting of experimental parameters under laboratory conditions usually hinders the accumulation of long time series required for a quantitative characterization of the dynamics in terms of statistical properties.

In this section, the first statistical characterization of chemical turbulence in catalytic CO oxidation on Pt(110) is presented based on an exceptionally long, stable experimental time series. Similar to the analysis in the previous section, the experimental data is transformed into phase and amplitude variables by the application of a Hilbert transform. From the phase representation topological defects are identified and their temporal behavior is analyzed statistically. For the mechanism of catalytic CO oxidation see Section 2.2.3. The experimental setup is described in Section 2.2.5.

3.2.1 Experimental data

The spatiotemporally irregular, turbulent states in catalytic CO oxidation on Pt(110) show a broad phenomenology. Most commonly, a state of *spiral wave turbulence* is encountered which is characterized by the spontaneous emergence of multiple rotating spiral wave fragments that move randomly and undergo breakups and mutual annihilation. In Fig. 3.8 (a), a series of four snapshots of spiral wave turbulence is displayed. However, the turbulent dynamics is highly sensitive to slight variations in partial pressures and temperature. Depending on the choice of parameters, the spiral fragments can be stronger developed and regular or the dynamics may be more disordered so that no spiral structures can be distinguished any more. An example of such a highly disorganized state is shown in Fig. 3.8 (b). Here, an irregular fine texture can be seen composed of randomly traveling, distorted, and constantly reshaping structures.

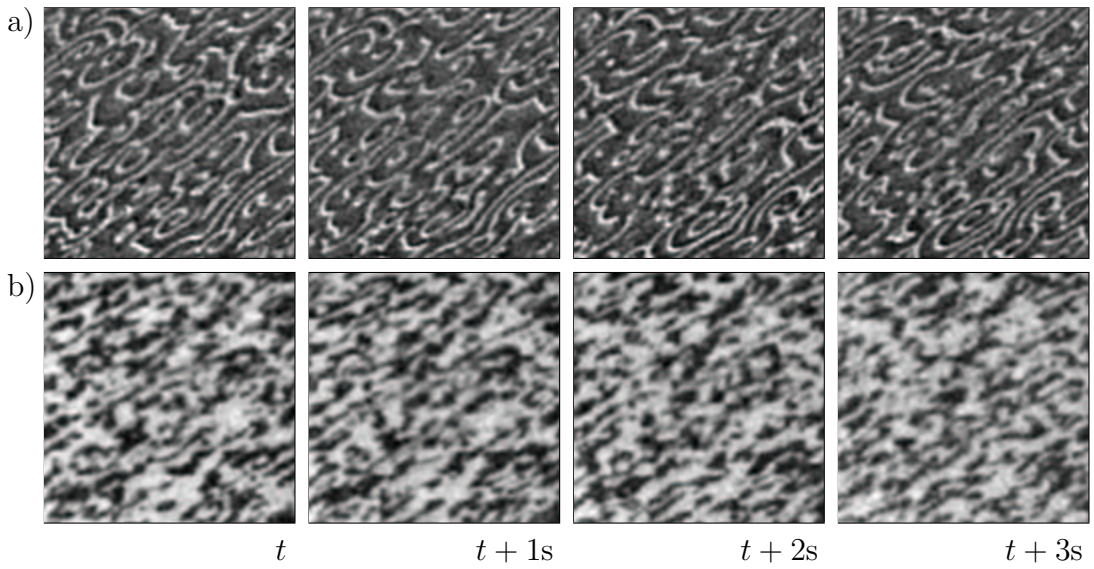

Figure 3.8: Chemical turbulence in catalytic CO oxidation on Pt(110). Two different examples, each represented by four subsequent PEEM images of size $330 \times 330\,\mu\text{m}^2$ taken at time intervals of 1 s. The parameters are (a) $T = 529\,\text{K}$, $p_{\text{O}_2} = 40.0 \times 10^{-5}\,\text{mbar}$, $p_{\text{CO}} = 12.3 \times 10^{-5}\,\text{mbar}$, and (b) $T = 502\,\text{K}$, $p_{\text{O}_2} = 40.0 \times 10^{-5}\,\text{mbar}$, $p_{\text{CO}} = 13.1 \times 10^{-5}\,\text{mbar}$.

The following analysis is based on the data set of Fig. 3.8 (b). The snapshots displayed in Fig. 3.8 (b) are taken from a time series of 12 min in length corresponding to 18 000 video frames (8-bit gray scale images of 300×300 pixel). Prior to the actual characterization of turbulent dynamics, standard image processing techniques are applied to enhance contrast and minimize the level of experimental noise. To smooth out temporal fluctuations the number of images is reduced by averaging over three adjacent frames yielding a series of 6000 images. Each image is then denoised by application of a 3×3 median filter and smoothed using a 5×5 boxcar average. Finally, a Butterworth high pass filter of order 7 with a frequency cutoff at $k = 1$ was applied to eliminate large scale modulations in the illumination of the PEEM images. The snapshots displayed in Fig. 3.8 have been processed in this way.

3.2.2 Topological defects

In Section 3.1.2, the turbulent data sets from a quasi-one-dimensional electrochemical system were characterized in terms of space-time defects that were identified from

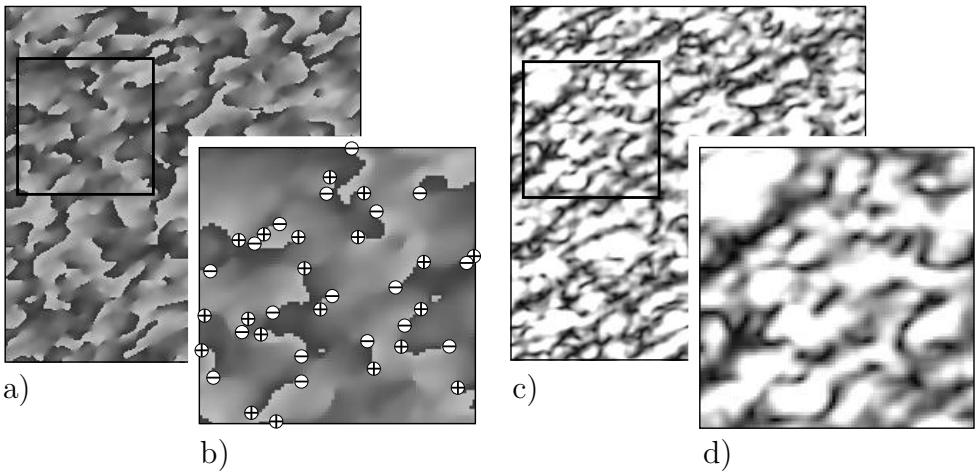

Figure 3.9: Phase (a,b) and amplitude (c,d) representations of the last frame in Fig. 3.8 (b). The frames (b) and (d) show zooms of selected regions of the phase and amplitude field, respectively, indicated by rectangular boxes. The images are coded in a linear gray scale color table, where white denotes high and black low values of the respective quantity. In (b), the locations of topological defects are marked with the symbols $\oplus$ and $\ominus$, depending on their topological charge.

a phase and amplitude representation of the data. Here, a similar approach is used to analyze the two-dimensional data from catalytic CO oxidation. A two-dimensional variant of the analytic signal approach is applied to transform the series of PEEM images into time-dependent spatial distributions of phase and amplitude. The details of this transform are explained in Appendix A.

In Fig. 3.9, the phase (a) and amplitude (c) fields corresponding to the last PEEM image in Fig. 3.8 (b) are displayed. For closer analysis of the details, the frames (b) and (d) show zooms of selected parts of the two images. From the phase image (a) it can be easily seen that topological defects are present. They are characterized by an integer topological charge m_{top}, *i.e.* along a closed contour surrounding the defect the phase changes by an amount of $2\pi\, m_{\mathrm{top}}$. More precisely, $m_{\mathrm{top}} = \frac{1}{2\pi} \oint \nabla\phi(\mathbf{r},t) \cdot d\mathbf{s}$ where $\phi(\mathbf{r},t)$ denotes the local phase at $\mathbf{r} = (x,y)$ and the integral is taken along a closed curve around the defect, see also the paragraph on spiral waves in Section 2.4.1. Thus, the defects correspond to end points of the equiphase contour lines in the phase image. Typically, only $m_{\mathrm{top}} = \pm 1$ is observed. In the zoom (b), the locations of defects are marked assigning the symbols $\oplus$ and $\ominus$ for topological charges of $+1$ and -1, respectively.

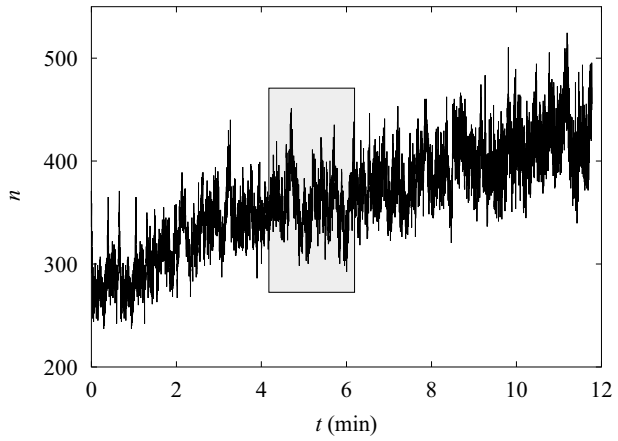

Figure 3.10: Number of defects n as a function of time. The gray shaded part is used for further statistical analysis. The parameters are as in Fig. 3.8 (b).

At the defect, the local amplitude drops to zero and the phase is not defined. From the amplitude image in Fig. 3.9 (c) it is obvious that the amplitude is significantly lowered at many locations. By careful inspection of the zoom in (d) and comparison with the corresponding phase image (b), the defects marked in (b) are found to coincide with locations of strongly reduced amplitude in (d). However, the minima in the amplitude field are not confined to the immediate positions of the defects. They can extend in the neighborhood of defects, so that larger regions of low amplitude emerge where several defects appear close to each other, as for instance on the left hand side of Fig. 3.9 (d). Besides, in some regions a reduced amplitude can be observed although no defect is present.

Number and positions of defects are therefore determined from the phase images. By use of finite differences, the gradient of the phase field is computed. As a topological defect is approached, the phase gradient diverges towards $\pm\infty$, depending on the sign of the topological charge. Thus, the positions and topological charges of defects can be identified by detecting strong positive and negative extrema in the gradient field. The entire time series of 6000 frames was analyzed by this procedure. The results were found to agree well with positions and topological charges expected from the termini of equiphase lines in the phase images. For example, the defects marked in Fig. 3.9 (b) were determined in this way.

In Fig. 3.10, the number of defects n is displayed as a function of time. Although the experimental conditions were kept constant throughout the entire recording, the dynamics is obviously changing. A steadily increasing average number of defects and

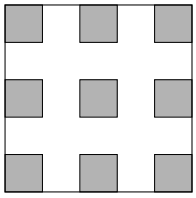

Figure 3.11: Choice of nine independent subsections of the system indicated by the gray shaded square regions. Each subsystem is $66 \times 66\,\mu$m in size.

growing fluctuations indicate that the system becomes more turbulent in the course of time. At present, the reason for this long term change in the behavior of the system is not known. A slow drift in the external parameters or a gradual change in the conditions of the single crystal surface could be responsible.

For further analysis a section of the time series around $t = 5\,$min is chosen, where the average number of defects remains stationary for some time. The selected subset of data starts at 4 minutes and 12 seconds and has a total length of 2 minutes corresponding to the gray shaded region in Fig. 3.10. In order to accumulate a sufficient amount of statistical data, nine identical independent subsections of the system are considered, the area of each subsystem being 1/25 of the total imaged surface area. In Fig. 3.11, the arrangement of the subsections is illustrated.

For the chosen interval of time, defects are counted within each of the nine subsystems. As an example, the number of defects in one subsection can be seen in Fig. 3.12 (a) as a function of time. Nine such time series obtained from the different subsections are combined to a single data set of about $N = 9000$ frames. From this set a mean

Table 3.1: Statistical properties of fluctuations in the number of topological defects.

		total	positive	negative
first moment	$\mu_1 = \frac{1}{N}\sum_i n_i$	17.05	8.57	8.48
second moment	$\mu_2 = \frac{1}{N}\sum_i (n_i - \mu_1)^2$	27.46	9.67	9.79
third moment	$\mu_3 = \frac{1}{N}\sum_i (n_i - \mu_1)^3$	69.93	20.74	21.56
fourth moment	$\mu_4 = \frac{1}{N}\sum_i (n_i - \mu_1)^4$	2500.09	351.08	389.66
fifth moment	$\mu_5 = \frac{1}{N}\sum_i (n_i - \mu_1)^5$	19996.56	2296.28	2917.88
skewness	$S = \mu_3/\mu_2^{3/2}$	0.49	0.69	0.70
kurtosis excess	$K = (\mu_4/\mu_2^2) - 3$	0.31	0.76	1.07

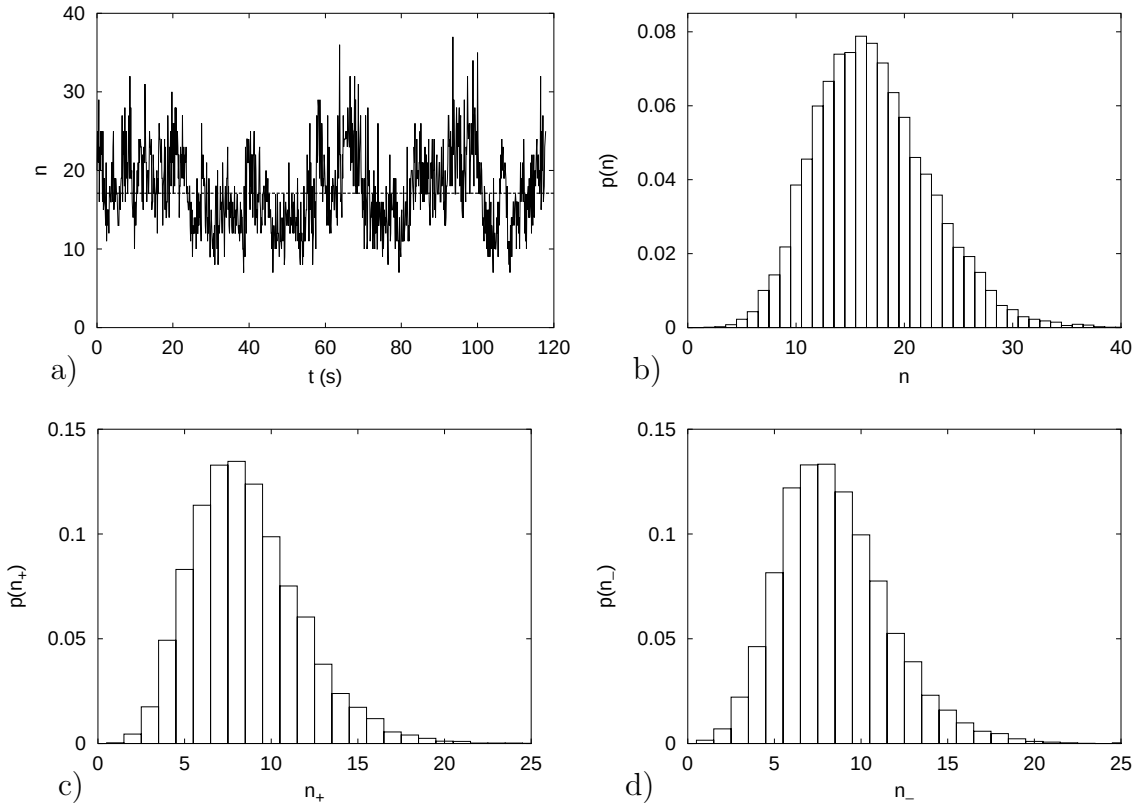

Figure 3.12: (a) Number of defects n as a function of time in one of the subsystems. The dashed line at 17.1 denotes the mean number of defects averaged over all frames of the nine subsystems. (b) PDF of the total number of defects n. (c) PDF of the number of defects n_+ with positive topological charge. (d) PDF of the number of defects n_- with negative topological charge. The distributions are accumulated over all nine subsystems.

value of 17 is obtained for the total number of defects, the mean for both the number of positive and negative defects being approximately 8.5. For the fluctuations around the mean value standard deviations of $\sigma = \sqrt{\mu_2} = 5.24$, $\sigma_+ = 3.11$, and $\sigma_- = 3.13$ are found for the total number of defects and the number of positive and negative defects, respectively. Higher central moments are listed in Table 3.1. Figures 3.12 (b), (c), and (d) show the probability distribution functions (PDFs) for each the total number of defects n and the number of positive and negative defects, n_+ and n_-, in an area of $66 \times 66\,\mu$m. The PDFs are positively skewed and slightly peaked compared to a normal distribution (leptokurtic). The respective values of skewness and kurtosis can be found in Table 3.1. Both skewness and kurtosis effects are more pronounced for the distributions of $n_\pm$ compared to the distribution of n.

3.2.3 Probabilistic model

In the following, a probabilistic model is derived to explain the experimental results that were presented in the previous section. The model is based on the approach of Gil *et al.* [182] who gave the first statistical description of defect turbulence in the CGLE. The master equation for the probability $p(n,t)$ of finding a number of n defects at time t in the observed area can be written as

$$\begin{aligned}\partial_t p(n,t) = {} & k_+(n-1)\,p(n-1,t) + k_-(n+1)\,p(n+1,t) \\ & - k_+(n)\,p(n,t) - k_-(n)\,p(n,t)\,,\end{aligned} \tag{3.1}$$

where $k_+(n)$ and $k_-(n)$ are the gain and loss rates of defects which may depend on the number of defects n. In the asymptotic regime, $\partial_t p(n,t) = 0$, Eq. (3.1) yields a simple recursive relation for the probability $p(n)$,

$$p(n) = \frac{k_+(n-1)}{k_-(n)}\,p(n-1)\,. \tag{3.2}$$

To derive an expression for the probability distribution from this equation, the gain and loss rates have to be found. Topological defects are created and annihilated in pairs of opposite topological charge. Therefore, in a system with periodic boundary conditions, the number of pairs is a convenient quantity for statistical characterization. In the present case, only a small fraction of a large extended system is considered. Here, defects can enter and leave the system by crossing the borders of the observed area. A full description would thus require to consider rates and distributions for both the number of positively and negatively charged defects, n_+ and n_-, simultaneously. However, to keep the analysis simple, it is assumed that $n_+ \approx n_-$ inside the observation window.

The gain and loss of defects is described on the basis of a simple model. It is assumed that there are two contributions to the rate of creation of defects. On the one hand, creation takes place constantly, depending only on the degree of turbulence, that is, on the choice of parameters. On the other hand, defects are known to replicate so that creation may be enhanced if more defects are present in the system [69]. Due to annihilation in pairs, the rate of annihilation is taken proportional to the square of the

number of defects. From these assumptions the gain and loss rates of defects can be written as

$$k_+(n) = c + d\,n \tag{3.3}$$

$$k_-(n) = a\,n^2\,, \tag{3.4}$$

where in the following n denotes the number of positive or negative defects, $n \equiv n_\pm$. Besides, c is the constant contribution to the rate of creation, $d\,n$ takes into account creation due to replication of defects, and $a\,n^2$ is the rate of annihilation. Inserting the expressions for k_+ and k_- into Eq. (3.2) the following probability distribution is obtained,

$$p(n) = Q\,\frac{\gamma^n\,\Gamma(\nu+n)}{(n!)^2} \tag{3.5}$$

with $\gamma = \frac{d}{a}$ and $\nu = \frac{c}{d}$. Normalization requires

$$Q = \frac{1}{\Phi(\nu,1;\gamma)\,\Gamma(\nu)}\,, \tag{3.6}$$

where Φ denotes the degenerate hypergeometric function. For details of the derivation of Eq. (3.5) see Appendix B. Note that for the case of $\nu = 1$, Eq. (3.5) turns into a Poisson distribution,

$$p(n) = e^{-\gamma}\,\frac{\gamma^n}{n!}\,. \tag{3.7}$$

However, the experimental result does not correspond to this particular situation, since for a Poisson distribution $\langle n\rangle = \sigma^2$, which is not fulfilled in the experiment.

The PDF (3.5) is now compared to the experimental PDF (Fig. 3.12) to evaluate the quality of the simple probabilistic assumptions (3.3) and (3.4). Since it is difficult to measure the parameters γ and ν directly from the experimental data, they are determined by fitting. To this end, it is required that the first and second moments of the PDF (3.5) are equal to the moments obtained from the experiment. The first two

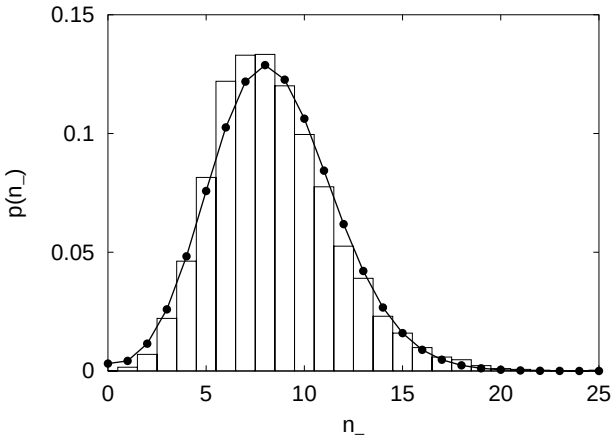

Figure 3.13: PDF of the number of negatively charged defects. The solid circles are a plot of $p(n)$ according to Eq. (3.5) for $n = n_-$ with $\gamma = 9.47$ and $\nu = 0.14$ determined from the experimental values of the first and second (raw) moments. The bars denote the experimentally obtained histogram and are identical to Fig. 3.12 (d).

(raw) moments of the distribution (3.5) are defined as

$$\langle n \rangle = \sum_{n=0}^{\infty} n\, p(n) = f_1(\gamma, \nu) \qquad \text{(mean)} \tag{3.8}$$

$$\langle n^2 \rangle = \sum_{n=0}^{\infty} n^2\, p(n) = f_2(\gamma, \nu)\,. \tag{3.9}$$

Analytic expressions can be obtained for both moments and are presented in Appendix B, Eqs. (B.13) and (B.14). They depend on the choice of γ and ν. Inserting the experimentally obtained values for the moments into Eqs. (3.8) and (3.9) two coupled equations for γ and ν are obtained. For the number of negative defects, $n = n_-$,

$$f_1(\gamma, \nu) = 8.48 \tag{3.10}$$

$$f_2(\gamma, \nu) = 81.68\,, \tag{3.11}$$

where the full expressions of $f_1(\gamma, \nu)$ and $f_2(\gamma, \nu)$ are given by (B.13) and (B.14). Equations (3.10) and (3.11) can be solved numerically yielding $\gamma = 9.47$ and $\nu = 0.14$. The values for γ and ν are then substituted into the theoretically derived PDF (3.5). Figure 3.13 shows the resulting plot of $p(n)$. It is superposed with the experimentally obtained histogram from Fig. 3.12 (d). The experimental data is well approximated by the distribution given in Eq. (3.5). A similar result is obtained for the PDF of n_+. Thus, although based only on a few general assumptions, the simple probabilistic model developed above shows good agreement with the experimental data.

3.2.4 Discussion

Spatiotemporally chaotic states dominated by topological defects can be observed in a variety of experimental systems and theoretical models. Well studied examples are known from fluid convection [62, 63, 184], electroconvection in liquid crystals [65], or nonlinear optics [185]. Besides catalytic CO oxidation, also other autocatalytic chemical reactions like the Belousov-Zhabotinsky reaction can exhibit defect-mediated turbulence [67]. Theoretical work mostly focused on the CGLE, where defect turbulence has been studied in detail [172, 181, 182, 186]. In the following, the probabilistic description of turbulence in catalytic CO oxidation on Pt(110) will be discussed in the context of similar statistical modeling reported in literature.

The first probabilistic characterization of defect turbulence was given by Gil *et al.* [182] for the regime of amplitude turbulence in the CGLE. They considered a system with periodic boundary conditions and assumed a constant rate of creation for pairs of topological defects, independent of the number of pairs m in the system. The rate of annihilation was taken proportional to m^2 since defects annihilate in pairs of opposite topological charge. On the basis of these two assumptions, a PDF for the number of defect pairs m can be derived that has the form of a square Poissonian,

$$p(m) = \frac{1}{I_0(2\sqrt{\gamma})} \frac{\gamma^m}{(m!)^2} \quad \text{with} \quad \langle m \rangle = \sqrt{\gamma}\, \frac{I_1(2\sqrt{\gamma})}{I_0(2\sqrt{\gamma})}\,, \quad \langle m^2 \rangle = \gamma\,. \tag{3.12}$$

Here, γ is the ratio of the gain and loss rate constants. The modified Bessel function of first kind I_j results from normalization. Moreover, it can be shown that in this case $\sigma^2/\langle n \rangle = 1$ if the number of defects n is of order 10.

Gil *et al.* showed that the theoretically derived square Poisson distribution (3.12) agrees well with the histogram of the number of defect pairs obtained from numerical simulations of the CGLE on a two-dimensional periodic domain [182]. Topological defects in a model for intracellular Ca^{2+} dynamics show a similar distribution as reported by Falcke *et al.* [187]. Recently, Davidsen and Kapral demonstrated numerically that a square Poisson distribution is also found for defect turbulence in systems where the local dynamics is chaotic [188]. Besides, the model of Gil *et al.* was also confirmed in experimental studies. Rehberg *et al.* obtained a square Poisson distribution for the

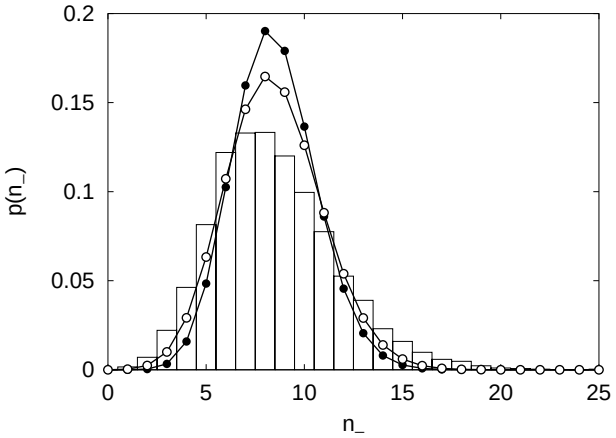

Figure 3.14: PDF of the number of negative defects. Square Poisson distribution [182] (filled circles) and modified Poisson distribution [63] (open circles) fitted to the experimental data. The bars denote the experimentally obtained histogram and are identical to Fig. 3.12 (d).

number of defect pairs from their experiments on defect turbulence in electroconvecting nematic liquid crystals [65]. In a later experimental work by Ramazza *et al.*, the statistics of topological defects in optical patterns was investigated [185]. Their result, however, does not unambiguously support the model of Gil *et al.* since the difference between Poissonian and square Poissonian fits lies within the experimental errors.

For comparison with the experimental data from catalytic CO oxidation, it is again assumed that $n_+ \approx n_-$, so that the number of defects pairs is equal to the number of positive or negative defects, $m = n_\pm$. From the experimental values of the moments, γ can be determined using the relation for $\langle n_\pm \rangle$ or $\langle n_\pm^2 \rangle$ given in Eq. (3.12). The matching with the experimental data is poor as can be seen in Fig. 3.14, where the square Poisson distribution for n_- is displayed in filled circles.

The approach of Gil *et al.* [182] was extended by Daniels and Bodenschatz in their statistical characterization of defect turbulence in inclined layer convection [63]. They took fluxes of defects across the system boundaries into account assuming a constant entering rate and a leaving rate proportional to the number of defects. Their assumptions are based on gain and loss rates determined from experimental data and lead to a modified Poisson distribution,

$$p(n) = \frac{1}{I_\nu(2\sqrt{\gamma})} \frac{\gamma^{(\nu/2)+n}}{\Gamma(\nu+1+n)\, n!}\,, \tag{3.13}$$

with n the number of positive or negative defects, $n \equiv n_\pm$. The modified Poisson distribution (3.13) turns into the square Poisson distribution (3.12) for $\nu = 0$. Although

their experimentally measured entering rate shows a weak dependence on n, the histogram of the number of defects from the inclined layer convection experiment agrees well with the distribution (3.13) [63, 189].

For the experimental data from catalytic CO oxidation the model of Daniels and Bodenschatz provides only a rough approximation. This is evaluated in the following way. Analytic expressions for the first and second moments can be derived from the distribution (3.13). They depend on γ and ν and their explicit form is given in Ref. [63]. Requiring these expressions to be equal to the moments of the experimental data, two equations similar to Eqs. (3.10) and (3.11) are given that determine the parameters γ and ν. The open circles in Fig. 3.14 show the modified Poisson distribution (3.13) obtained from this fit. Even though the matching is improved with respect to the square Poisson distribution (3.12), the agreement with the experimental histogram is not satisfactory. The PDF derived in the previous section yields a considerably better approximation of the experimental result (cf. Fig. 3.13).

Apart from the CGLE, defect turbulence has also been studied theoretically using various other reaction-diffusion models. Here, a FitzHugh-Nagumo type model is of particular interest that shows a spiral breakup scenario leading to chemical turbulence [85, 190]. It can be regarded as a reduced version of the realistic reaction model for catalytic CO oxidation described in Section 2.2.4. On the basis of numerical simulations of this model, the concept of Gil *et al.* has been generalized in a theoretical work by Hildebrand *et al.*, taking into account the influence of spatial correlation between defects [147]. They considered a transition from rotating spiral waves to defect-mediated space-time chaos. In the vicinity of the Hopf bifurcation, the ratio of variance and mean of the number of defects, $\sigma^2/\langle n\rangle$, is unity in agreement with the result of Gil *et al.*. Towards the spiral breakup transition this ratio decreases to zero. The results were explained by analyzing the pair correlation functions of defects. Close to the transition, the creation of defects in the vicinity of existing ones is highly unlikely, while further within the turbulent regime the strong anticorrelation between defects vanishes. For the experimental data analyzed here a ratio of $\sigma^2/\langle n\rangle = 1.61$ is found. Assuming that the model used by Hildebrand *et al.* applies to the present case, it can be concluded that the dynamical state of the experimental system is far from the spiral breakup transition. However, spatial correlations between defects are present to some extent

and probably responsible for differences between the experimental histogram and the PDF derived from the simple statistical model that can be seen in Fig. 3.13.

In summary, the statistics of defect-mediated turbulence in catalytic CO oxidation on Pt(110) may be described by a simple probabilistic model that can be considered as a refined version of the approach of Gil *et al.* [182]. Besides a constant contribution to the rate of creation, replication of defects is taken into account to get good agreement with the histogram of the number of defects from the experiment.